JGR Atmospheres

RESEARCH ARTICLE
10.1029/2019JD031226

Regional Differences of Chemical Composition and Optical Properties of Aerosols in the Tibetan Plateau

Jianzhong Xu[1], Anusha Priyadarshani Silva Hettiyadura[2], Yanmei Liu[1], Xinghua Zhang[1], Shichang Kang[1], and Alexander Laskin[2]

[1]State Key Laboratory Cryopheric Sciences, Northwest Institute of Eco-Environment and Resources, Chinese Academy of Science, Lanzhou, China, [2]Department of Chemistry, Purdue University, West Lafayette, IN, USA

Key Points:
- Collected $PM_{2.5}$ filter samples from Tibetan Plateau were analyzed to examine the regional differences in aerosol properties.
- The optical properties of water-soluble organic carbon (WSOC) from the south show higher light absorption than those collected at the north.
- The molecular-level chemical composition shows significant differences in WSOC composition representative of two sampling sites.

Supporting Information:
- Supporting Information S1

Correspondence to:
J. Xu,
jzxu@lzb.ac.cn

Citation:
Xu, J., Hettiyadura, A. P. S., Liu, Y., Zhang, X., Kang, S., & Laskin, A. (2020). Regional differences of chemical composition and optical properties of aerosols in the Tibetan Plateau. *Journal of Geophysical Research: Atmospheres*, *125*, e2019JD031226. https://doi.org/10.1029/2019JD031226

Received 23 JUN 2019
Accepted 4 DEC 2019
Accepted article online 18 DEC 2019

Author Contributions:
Data curation: Anusha Priyadarshani Silva Hettiyadura, Yanmei Liu, Xinghua Zhang
Funding acquisition: Shichang Kang, Alexander Laskin
Methodology: Yanmei Liu, Xinghua Zhang
Supervision: Shichang Kang, Alexander Laskin
Writing - original draft: Jianzhong Xu
Writing – review & editing: Anusha Priyadarshani Silva Hettiyadura, Alexander Laskin

Abstract In this study, $PM_{2.5}$ filter samples were collected from two high-elevation sites located in the southern and northern areas of Tibetan Plateau (TP): the Qomolangma Station for Atmospheric Environmental Observation and Research (QOMS) and Waliguan Baseline Observatory (WLG), respectively. Collected samples were analyzed to examine the regional differences in aerosol properties and relate them to potential chemical processes in the TP area. The aerosol mass concentrations inferred from measured chemical components were higher at WLG (11.2 μg m^{-3}) compared to QOMS (6.8 μg m^{-3}). The chemical composition shows higher contribution of organic aerosol at QOMS than that of WLG. The optical properties of water-soluble organic carbon (WSOC) from the QOMS samples show higher light absorption efficient than those collected at WLG. The light absorption of WSOC at QOMS indicates significant pH dependence with enhanced light absorption at higher pH values, while the light absorption of WSOC from WLG samples show very weak pH dependence. The different pH dependence property suggests the different chemical composition between them. The molecular-level chemical composition investigated using high-resolution mass spectrometry (HRMS) assisted with an electrospray ionization (ESI) shows significant differences in WSOC composition representative of two sampling sites. For QOMS samples, CHO and CHON compounds are the major chemical species detected in the negative (−) ESI mode, while CHO and CHOS compounds are the most abundant chemical species detected by the same method in samples collected at WLG. The differences in their molecular composition indicate the different sources and chemical processes in these two regions.

1. Introduction

Tibetan Plateau (TP) is the biggest mountain plateau in the world with an area of ~2,500,000 km^2 and average elevation more than 4,000 m above sea level (a.s.l), which impacts the regional climate and environment through various dynamic and thermal effects (Yanai & Wu, 2006). The radiative energy balance over TP is an important component of its thermal effect which is substantially influenced by ambient aerosol composition and concentration (Lau et al., 2006). Light absorbing carbonaceous species are important components of local aerosol, defining its direct radiative climate forcing in the area (Ramanathan et al., 2007). Because of the large scale of the TP area, the aerosol content and composition over the TP is very diverse.

The aerosol composition in the northern and southern TP is expected to be significantly different owing to differences in emission sources, climate systems, and meteorological conditions. Satellite observations indicate frequent aerosol transport from the northwestern South Asia during March to June (pre-monsoon period) every year to the southern TP (e.g., Himalayas) (Liu et al., 2008), and from the northwestern China and Central Asia during summer in the northern TP (Huang et al., 2007). Specifically, enhanced thermal mountain-valley circulation is dominated in the northern TP during summer and drive aerosol plume to the high-elevation regions, while the southern TP is less polluted during summer because of the rapid wash-out of aerosol by frequent precipitation in the low elevation regions (Bonasoni et al., 2010; Hegde & Kawamura, 2012; Xu et al., 2013). Favorable conditions for aerosol transport to the southern TP are in the pre-monsoon period when westerly winds and high aerosol loading at the source region are coupled together. In addition, use of different fuels in two regions has a substantial impact on the aerosol composition and its variability between the southern and northern TP. Carbon isotope analysis of black carbon (BC) in the northern TP indicated sources from fossil fuel combustion, whereas BC sources in the southern TP

were attributed to biomass burning emissions (Li et al., 2016). However, the overall chemical and optical characteristics of aerosol representative of the southern and northern TP regions are yet insufficiently investigated.

Recent studies conducted in the southern and northern TP characterized the overall chemical composition and mass loading of aerosols in these areas (e.g., Bonasoni et al., 2010; Marcq et al., 2010; Xu et al., 2014). The average mass loadings of $PM_{2.5}$ are generally lower at TP (<10 $\mu g\ m^{-3}$) compared with urban areas (>70 $\mu g\ m^{-3}$) in China due to remote location and high elevation of TP. However, long-range transport events bringing much higher concentrations of $PM_{2.5}$ were also reported with the mass loading up to 30 $\mu g\ m^{-3}$ (Lüthi et al., 2015; Xu et al., 2014). Water-soluble inorganic ions were analyzed as components of aerosol chemical composition, attributing them to common anthropogenic activities (Xu et al., 2014). Carbonaceous content of aerosol has been a subject of recent studies due to its important contribution to mass loading and significant climate effects (Cao et al., 2009). Measurements of the organic to elemental carbon ratio (OC/EC) show elevated organic content in the southern TP attributed to the aged biomass burning emissions (Ming et al., 2010). Aerosol mass spectrometry (AMS) has been applied in field studies of the aerosol chemistry which reported description of main organic aerosol (OA) classes, their temporal variations, variability in chemical composition, sources, and oxidation states (Xu et al., 2018; Zhang et al., 2018). Molecular characterization of volatile OA fractions has been reported based on the gas-phase MS measurements and provided further insights on OA sources and chemistry (Hegde & Kawamura, 2012). However, most of these studies were conducted at the southern TP locations, and less studies were performed at the northern TP.

Light absorption property of aerosol is important for evaluating its direct radiative forcing in the atmosphere. Light absorbing components of OA (aka Brown carbon, BrC) absorb light at the low visible to near-ultraviolet (UV) wavelength range, and the BrC composition and sources have been a subject of many studies in recent years (Laskin et al., 2015). The light absorption by BrC is expected to increase with altitude because BrC can be transported to high altitudes by deep convection, and it can be also formed by in-cloud multiphase reactions (Zhang et al., 2017). The optical properties of BrC are also dependent strongly on the fuel types (Olson et al., 2015). Generally, more absorbing BrC is typical for biomass burning organic aerosol (BBOA) and anthropogenically influenced secondary organic aerosol (anthropogenic SOA) (Washenfelder et al., 2015; Zhang et al., 2011). Molecular-level studies of BrC composition show that the light absorbing compounds are polycyclic aromatic hydrocarbons (PAH) and their oxygenated derivatives, nitroaromatics, phenols, and aromatic acids (Desyaterik et al., 2013; Lin et al., 2016; Lin et al., 2017; Lin et al., 2018; Xie et al., 2017). Furthermore, light absorbing spectral properties of BrC are pH dependent, which is important for evaluating the ambient radiative forcing in modeling studies (Lin et al., 2017; Phillips et al., 2017). Although the contribution of BrC to light absorption is widely characterized in urban environments around the world, information on the BrC composition and optical properties pertinent to the TP is scarce.

In this study, we extract and analyze the water-soluble organic carbon (WSOC) in aerosol samples collected at two field sites, located at the southern and northern edges of TP using a suite of methods including high-resolution mass spectrometry (HRMS), giving insights to chemical composition and optical properties of water-soluble BrC. Furthermore, this study sheds light on plausible sources of WSOC and aging of OA at these two sites.

2. Materials and Methods

2.1. Sample Collection

The first set of aerosol samples were collected during a pre-monsoon period on 12 April 12 to 12 May 2016 at the Qomolangma Station (QOMS, 28.36°N, 86.95°E, 4276 m a.s.l), a remote comprehensive research observatory located at the toe of Mt. Qomolangma (Everest) of north Himalayas (Zhang et al., 2018). The second set of the aerosol samples were collected at Mt. Waliguan Baseline Observatory (WLG, 36.28°N, 100.9°E, 3816 m a.s.l) during a separate field study conducted on 1–31 July 2017 (Zhang et al., 2019). Figure 1 shows the location of QOMS and WLG sites on a map of the TP region. The sampling periods at both sites were during "high aerosol" periods typical for the area. Since these two sites are all located at the elevated remote areas, the collected samples contain aerosol-transported long distances from the emission sources. A suite of online instruments was co-located during each study as reported elsewhere (Zhang et al., 2018; Zhang et al., 2019). Aerosol filter samples at each site were collected on prebaked

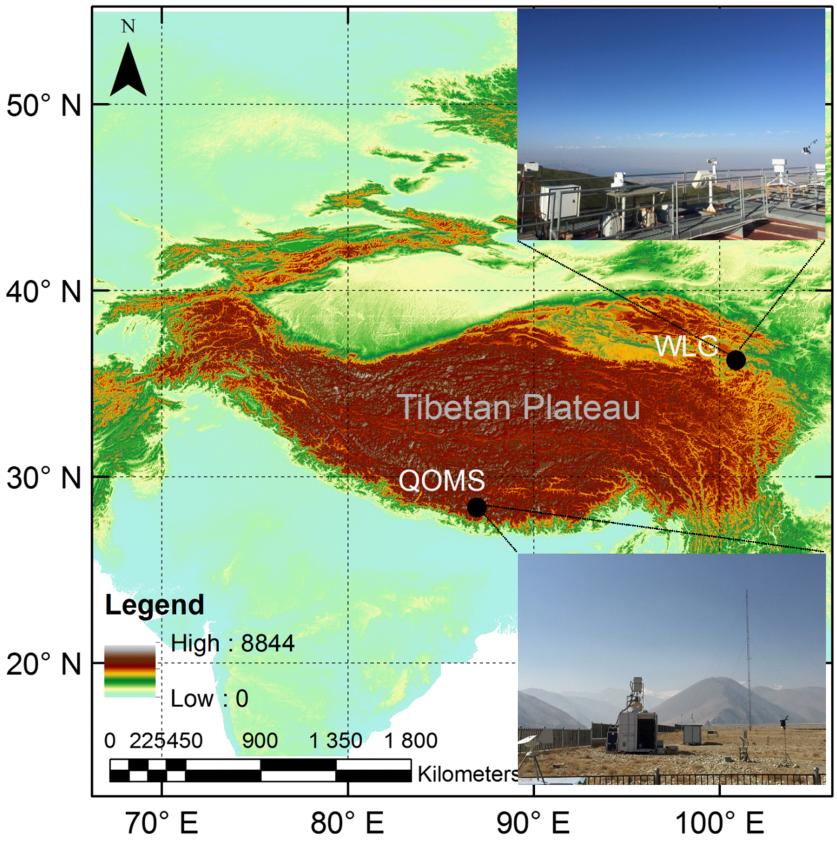

Figure 1. Location map for the Tibetan Plateau and two sampling sites (QOMS and WLG). The insert photos for each site were taken during field study.

quartz-fiber filters (47 mm diameter, Tissuquartz 2500 QAT-UP, PALL Life Sciences) with a low volume $PM_{2.5}$ filter sampler (16.7 L min^{-1}, model PQ200, BGI, USA). Each filter sample was collected every 48 hr, starting at around 8:00 am (LT). Table S1 lists a total of 15 and 16 filter samples collected during the QOMS and WLG studies, respectively. Blank filter samples were also obtained at each of the sites by placing the filter in the sampler for 10 min without flowing air through the filters. The flow rates in each of the samplers and corresponding meteorological conditions were recorded at 5 min intervals. The total volumes of air filtered to collect the samples ranged between 37 and 48 m^3 at the ambient condition. After collection, the samples were placed in hermetic containers and stored at −20 °C in the dark pending analysis.

2.2. Overall Chemical Composition Analysis

The filter samples (11.95 cm^2 of total area) were analyzed for basic chemical components. First, a 0.526 cm^2 portion of each filter was analyzed for OC and EC content using a Thermal/Optical carbon analyzer (Desert Research Institute [DRI] Model 2001, Atmoslytic Inc., Calabasas, CA, USA). The remaining filter was extracted in Milli-Q water (TOC < 5 ppb, 18.2 M Ω·cm) or LC-MS grade water (Fisher Scientific, USA) using an ultrasonic bath for 30 min. The ultrasonic bath was kept at low temperature through adding ice in the ultrasonic bath to prevent chemical reactions and evaporation loss during sonication. The extraction efficiency of this method is estimated as 50%–70% based on previous study (Bein & Wexler, 2014). At the next step, water-insoluble residuals were removed by filtering extracts through 0.45-μm pore-size PTFE Acrodisc syringe filter (Pall Life Sciences). The water-soluble extracts were then analyzed for concentrations of selected inorganic ions (Na^+, NH_4^+, K^+, Mg^{2+}, Ca^{2+}, Cl^-, SO_4^{2-}, and NO_3^-) using a dual ion chromatograph system, following protocols described elsewhere (Xu et al., 2015). WSOC was analyzed by a carbon analyzer (model Vario Cube, Elementar, Hanau, Germany). Fractions of WSOC were calculated by subtracting inorganic carbon (IC), which is the sum of carbon in carbonates and dissolved CO_2 in the sample, from total carbon (TC). Fractions of water-insoluble organic carbon (WIOC) were calculated as the difference of

OC and WSOC mass concentrations. The details of instruments and measurement procedures are published elsewhere (Feng et al., 2016; Lin et al., 2018; Xu et al., 2015).

Light absorbance of WSOC extracts was measured using a UV-visible (UV-vis) spectrophotometer (Model UV-2700, Shimadzu, Kyoto, Japan). Absorption spectra of WSOC extracts were acquired in the range of 200 to 900 nm at 1 nm intervals using Milli-Q water as the reference. The absorption spectra were baseline corrected by subtracting the mean absorbance from 690 to 700 nm. All absorption data in this study were converted to an absorption coefficient at a given wavelength (Abs_λ). These absorbance values were used to compare the absorption feature at these sites and derive the imaginary part of the complex refractive index of water-soluble BrC. In order to investigate the potential photo-blenching of BrC and chemical difference between these two sites, a photolysis experiment was conducted by illuminating the water extracts in a 1-cm quartz cuvette for 4 hr using an ultraviolet light-emitting diode (LED, Thorlabs, M365LP1, Ocean Optics). The LED emission spectrum was centered at 365 nm with a bandwidth (FWHM) of 9 nm. The LED was mounted about 30 cm up cuvette resulting in an incident power density of ~5 mW cm^{-2}. Meantime, the light absorption of water extracts was measured online using a broadband (180–900 nm) light source at 30-s interval (DH-2000, Ocean Optics).

2.3. pH-Dependent Measurement

Samples with highest mass loadings at each site were selected to record their UV-vis absorption spectra at different pH settings. Specially, four samples (F1, F29, F31, and F44) from QOMS and three samples (F1, F4, and F9) from WLG were selected based on their mass concentrations (Table S1), concurrent AMS records of aerosol composition, and air backward trajectory analysis confirming characteristic long-range air transport at each site. The pH of the sample was adjusted using mixtures of HCl (0.01 M) or NaOH (0.5 M) solutions added using a micro-pipette. The pH value of each sample was adjusted from 2 to 12, as measured by a pH meter (Orion Star A111, Thermo Fisher Scientific, Waltham, MA, USA). The pH meter was calibrated with buffer solutions of pH 4.01, 7.00, and 10.01 during the measurement.

2.4. HRMS Molecular Analysis

Organic aerosol is a very complex mixture, and HRMS is the most powerful tool for the OA characterization (Laskin et al., 2018). In this study, molecular characterization of WSOC was performed using a Q-Exactive HF-X Orbitrap™ mass spectrometer (Thermo Scientific, Inc.). The WSOC extracts were concentrated and de-salted using solid phase extraction (SPE) cartridges (DSC18, Supelco). The cartridges were conditioned using a one-column volume of acetonitrile (Optima®, Fisher chemical) and a one-column volume of ultrapure water (LC/MS grade, Fisher Chemical), respectively. The acidified sample (pH = 2) went through the cartridge at a low flowrate and eluted with a one-column volume of ultrapure water first to remove the loosely bound salts and then with a one-column volume of acetonitrile to elute the organics that were retained on the cartridge. The efficiency of the SPE cartridges was evaluated by measuring the UV-vis absorption before and after filtering and was found to be above 50%. Small molecular acids and carbohydrates may not be retained by the SPE cartridge and likely they were removed with the salts. The acetonitrile fractions were concentrated to 2 mL under a slow stream of ultra-pure N_2 gas.

Prior the HRMS analysis, 0.5 mL of the sample was combined with 0.5 mL of methanol in 10% water. The samples were directly infused to the mass spectrometer using an electrospray ionization source (ESI) operated in either positive or negative mode. The samples were injected at a flow rate of 5 μL min^{-1}. HRMS spectra were acquired at a mass range 80–1,200 Da, mass resolving power of 240,000 at m/z 200. Spray voltages of −2.5 and +3.5 kV were used in negative and positive ionization modes, respectively.

2.5. HRMS Data Process

The experimental data files were acquired using Xcalibur software (Thermo Scientific), and individual MS peaks were extracted using Decon2LS program (http://ncrr.pnl.gov/software/). Background subtraction and further data processing were performed using custom-made Microsoft excel macros (Roach et al., 2011). Briefly, the HRMS data were background subtracted using a blank, and the formula assignment was performed based on the first- and the second-order Kendrick mass defects using the macros and a formula calculator (V1.1, MIDAS Analysis), excluding ^{13}C isotopes. The formula assignment was limited by <2 ppm mass accuracy filter. The formula assignments considered the following set of elements $C \leq 50$,

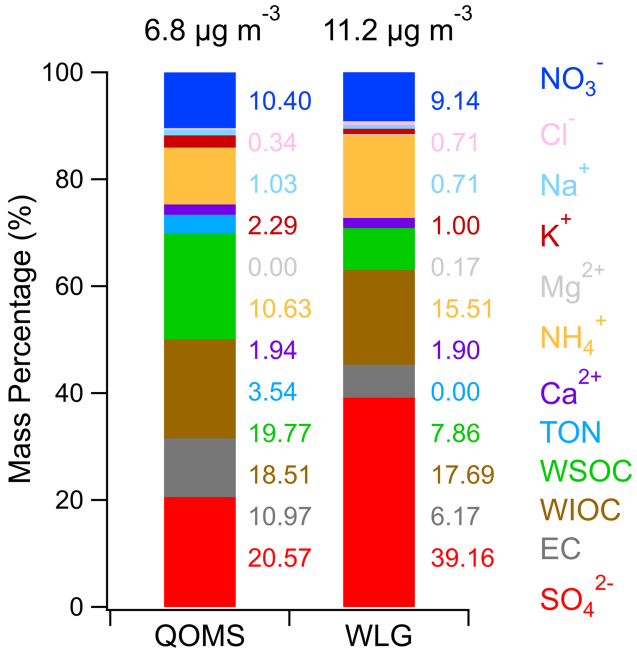

Figure 2. The average mass concentration (top), chemical composition (colored) and contribution (right of column) of $PM_{2.5}$ filter samples at each sampling site collected during 12 April to 12 May 2016 for QOMS and 1–31 July 2017 for WLG.

O ≤ 40, H ≤ 50, N ≤ 4, S ≤ 1, and Na ≤ 1 (positive mode only). The formula assignments were also constrained by elemental ratios of 0.3 ≤ H/C ≤ 3.0, 0.0 ≤ O/C ≤ 3.0, 0.0 ≤ N/C ≤ 0.5, 0.0 ≤ S/C ≤ 0.2, and the double bond equivalent (DBE) of 0.0 ≤ DBE/C ≤ 0.9.

3. Results and Discussions

3.1. Aerosol Mass Loadings and Main Chemical Fractions

The $PM_{2.5}$ average mass concentration reconstructed from chemical measurements are 6.8 μg m^{-3} for QOMS and 11.2 μg m^{-3} for WLG (Figure 2). This trend is consistent with the PM_1 mass loadings reported by AMS measurements at these sites (4.4 μg m^{-3} for QOMS and 9.1 μg m^{-3} for WLG) (Zhang et al., 2018, 2019). The mass difference between $PM_{2.5}$ and PM_1 were from the different size cut and their chemical composition (such as mineral dust cannot be detected by AMS). The particle-type composition of aerosols from these two sites was also significantly different. The chemical composition of $PM_{2.5}$ from the WLG samples was dominated by sulfate, followed by ammonium, WIOC, WSOC, nitrate, EC, and other chemical species. In contrast, main chemical fractions of QOMS samples were in the order of WSOC, WIOC, sulfate, ammonium, EC, nitrate, and other chemical species (Figure 2). The high contribution of sulfate at WLG was also reported in other studies conducted at the northern TP (Xu et al., 2014; Zhang et al., 2014). While $PM_{2.5}$ in QOMS is neutral, $PM_{2.5}$ in WLG was weakly acidic based on the ion charge balance between ammonium and sum of sulfate and nitrate (Figure 3). The ratio of EC/OC, which is an index for the organic matter oxidation, were similar for these two sites (0.17 and 0.18) (Figure 3). The ratio of WSOC/OC was consistent within all QOMS samples, whereas it showed two distinct ratios for the WLG (Figure 3) samples, suggesting substantial differences in aerosol sources and chemical processing.

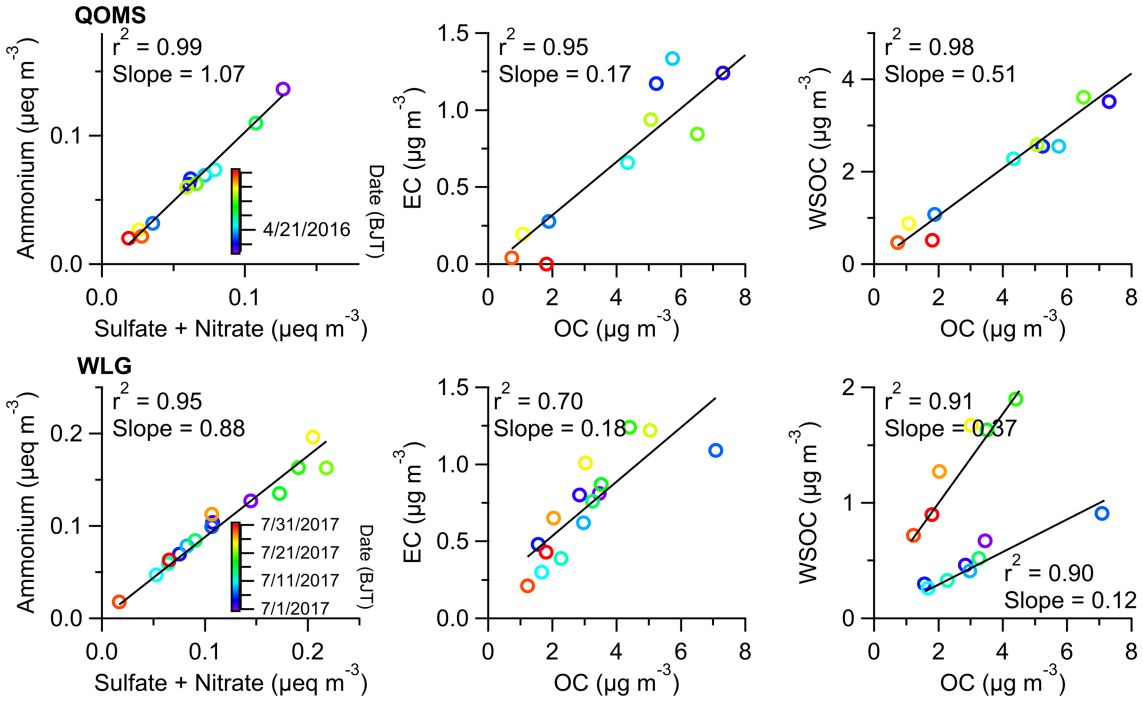

Figure 3. Scatter plots for ammonium vs. the sum of sulfate and nitrate, EC (elemental carbon) vs. OC (organic carbon), and WSOC (water-soluble OC) vs. OC in $PM_{2.5}$ samples collected from each sampling site (QOMS; top plane, WLG; bottom plane).

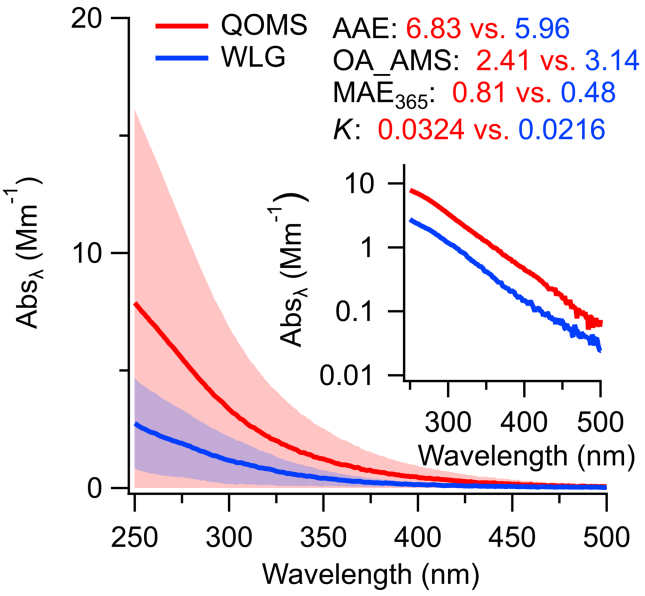

Figure 4. The average light absorption of WSOC (water-soluble organic carbon) in QOMS and WLG. The shaded area for each average absorption spectrum represents one-time standard deviation (1σ). The insert figure shows the average absorption spectrum at log scale. The values of AAE (absorption Ångström exponent between 300 and 400 nm), OA_AMS (organic aerosol measured by AMS), mass absorption coefficient (MAE) at 365 nm (MAE_{365}), and the imaginary part *k* of refractive index are also shown.

3.1.1. Light Absorption Properties of WSOC

The average absorption coefficient spectra of filter extracts as a function of wavelength (nm) for both sites are shown in Figure 4. The absorption coefficient of WSOC at QOMS was significantly higher than that of WLG although the concentration of WSOC at QOMS was lower than that at WLG. Quantitatively, the absorption coefficient at 365 nm ($Abs_{365} \pm 1\sigma$) was 0.92 ± 0.97 for QOMS and 0.30 ± 0.23 for WLG, respectively. The absorption variation with respect to wavelength (AAE; absorption Ångström exponent) was determined from the slope of a linear regression fit of base 10 absorption coefficient versus wavelength within the range of 300 to 400 nm. AAE was slightly higher for QOMS than WLG (6.83 vs. 5.96), suggesting potential difference in the chemical composition of BrC. Similar results (AAE: ~5.0) were also observed in Himalayas during pre-monsoon (Kirillova et al., 2016) and the southeastern TP (AAE: 6.9) (Zhu et al., 2018). Values of the mass absorption efficient at 365 nm (MAE_{365}), calculated from the ratio of the absorption coefficient at 365 nm and mass concentration of WSOC, recorded for the samples from these two sites, were 0.81 for QOMS and 0.48 for WLG, respectively. The MAE_{365} of the QOMS samples in our study is similar to that reported previously (0.66–0.72 $m^2\ g^{-1}$) for the same area of study—the Himalayas (Kirillova et al., 2016). These MAE_{365} values are significantly lower than those characteristic for fresh and/or less aged aerosol in urban areas of Beijing during winter (1.26), but close to the values reported during summer (0.52) (Du et al., 2014). The MAE_{365} value of the QOMS samples was higher than that typical for aerosol in urban and rural sites (0.13–0.53) of the southeastern United States (Liu et al., 2013). The MAE_{365} value of the WLG samples is at a low range of literature results. Accordingly, the imaginary part k of refractive index, which is directly related to light absorption by aerosol and can be incorporated into climate models, was 0.0324 for the QOMS and 0.0216 for the WLG samples, estimated based on the density of OA from AMS results using element ratio method (1.4 g cm^{-3} for the QOMS and 1.6 g cm^{-3} for the WLG samples, respectively; $\rho_{org} = 1000 * [(12 + 1 * (H:C) + 16 * (O:C)]/[7.0 + 5.0(H:C) + 4.15 * (O:C)]$) (Kuwata et al., 2011). Overall, the light absorbance of OA measured at the QOMS site is high enough that the radiative heating could be significant in this mountain area (Jo et al., 2016).

3.1.2. Effect of pH on Light Absorption

Recent studies showed that the light absorption by some of the BrC samples is pH dependent due to deprotonation or conformational changes on chromophores at high pH values (Lin et al., 2017; Phillips et al., 2017). In this study, we also investigated the effect of pH on light absorption for the high mass concentration samples from QOMS and WLG. The results are shown in Figure 5. Absorbance of the QOMS sample showed a significant increase with the increase of pH, compared to the absorbance by the WLG sample. The integrated absorbance between 300 and 450 nm normalized to pH = 2 at QOMS showed a clear increase with a slope of 0.07 (Figure 6a). This slope was consistent with the observation for a forest fire aerosol sample in Phillips et al. (2017) (0.08). The pH dependent absorption spectra for QOMS are also clearly illustrated by the ratio of the average absorption at different pH values, with respect to the absorption at pH = 2 (Figure S1). The AAE values (within the range 300 to 450 nm) for QOMS samples decrease with the increase of pH (Figure S2) indicating that absorption of BrC at longer wavelengths increased more than at shorter wavelengths. This phenomenon was observed for BrC components such as nitroaromatic species (Lin et al., 2017) and humic substances (Phillips et al., 2017) due to red-shifting absorption under the roles of deprotonation and conformational changes of these compounds. However, this was not observed for BrC at WLG. Furthermore, subtle changes at different wavelengths for different samples at QOMS were also observed by the plot of difference between the absorbance at a particular value of pH related to pH = 2 (Figure S3), suggesting presence of different chromophores in different samples (Phillips et al., 2017). Overall, the observed effects of pH on the BrC absorption pertaining to the QOMS and WLG samples suggest differences in the chemical composition of BrC at two sites.

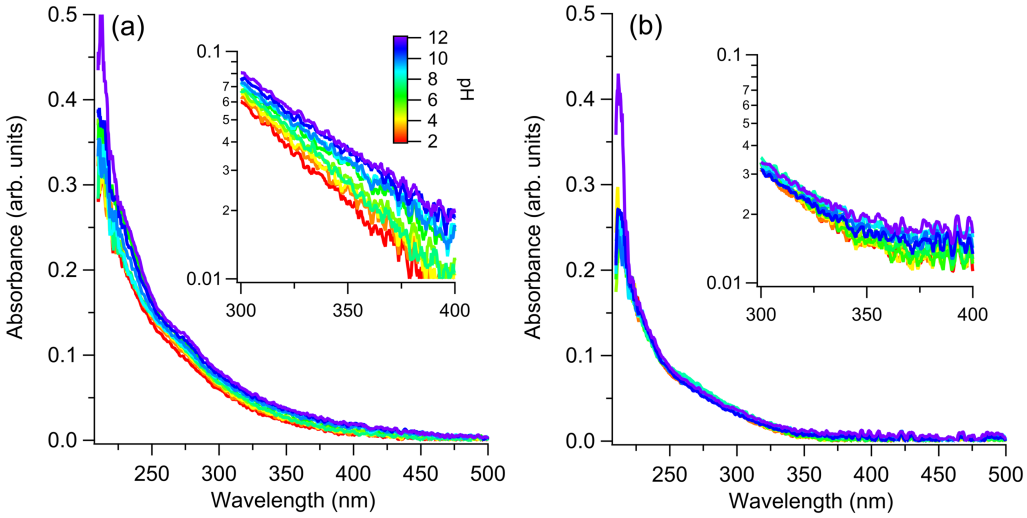

Figure 5. Averaged absorbance spectra as a function of pH for the WSOC samples from (a) QOMS and (b) WLG. The linearity of the log-transformed spectra (inset) indicates the quality of fit to a power law function.

3.1.3. Photolysis of WSOC

To assess stability of WSOC under photolysis, the extracts were photolyzed at a 365 nm light for 4 hr. The overall characteristics of this experiment was substantial photobleaching at the short wavelengths (300–350 nm), although the extent of this effect varied (Figure 7). The observed photobleaching effect suggests that aerosol at QOMS and WLG had experienced strong aging during transport to the sampling site. Lin et al. (2016) reported a ~16 hr half-time of photolytic decay for water extract of fresh biomass burning aerosol at a natural light condition. For ambient aerosol, there were many oxidants in the atmosphere; therefore, the photolytic decay could be faster than the reported half time (Fleming et al., 2019). In addition, since the photolytic decay experiment was conducted for water extract, in which the initial pH was close to neutral, the photolytic decay could be faster under acidic condition which is more consistent with the actual ambient conditions (Cai et al., 2018). The photolytic decay for the sample from WLG is not a smooth exponential decay, likely because different chromospheres decompose at different rates (Fleming et al., 2019).

3.2. Molecular-Level Insights into WSOC

The reconstructed (+)ESI and (−)ESI mass spectra showing the assigned m/z for (a) QOMS and (b) WLG samples are displayed in Figure 8. The fractions of the assigned formulas to the total detected MS peaks were in the range of 41%–50% in each of the experiments. Majority of the formulas were detected in (−)ESI mode

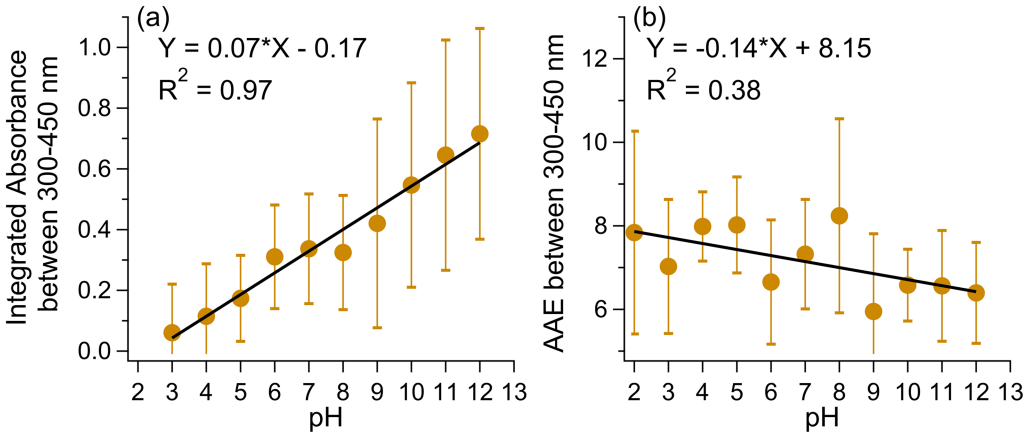

Figure 6. (a) Integrated absorbance (300–450 nm) normalized to values at pH = 2 as a function of pH and (b) absorption Ångström exponent (AAE) as a function of pH for samples of QOMS. The error bar is the standard deviation (1σ).

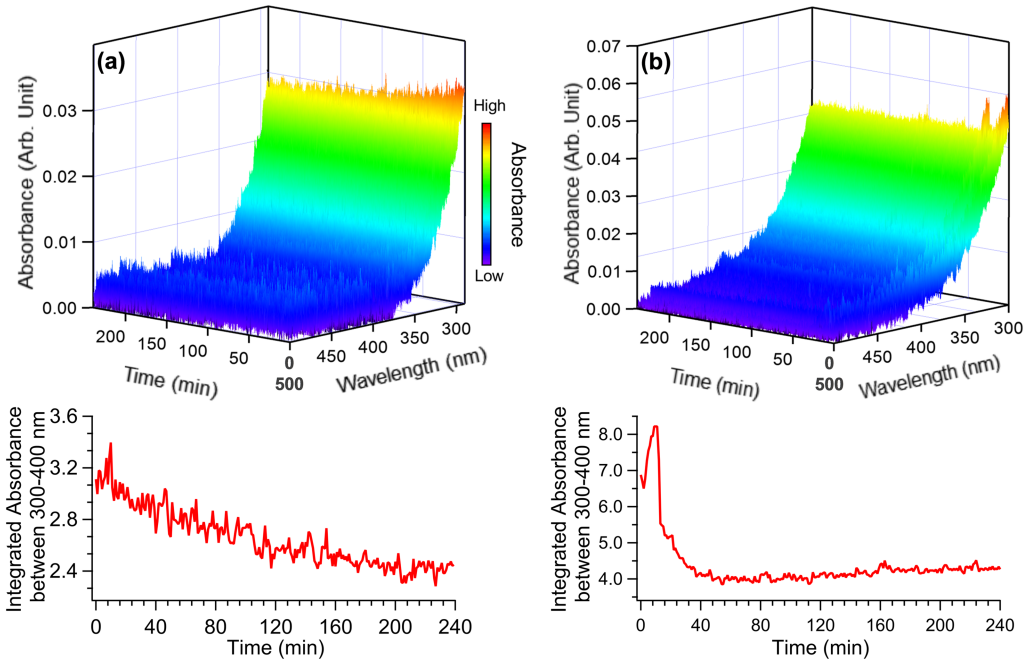

Figure 7. Photolysis of high mass concentration samples at (a) QOMS and (b) WLG

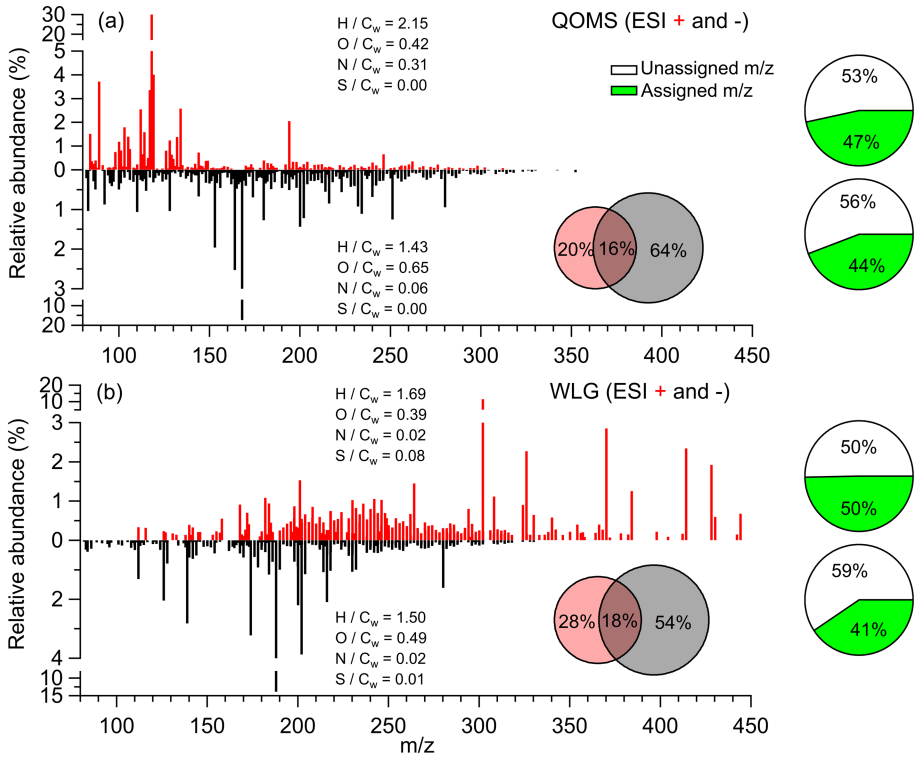

Figure 8. The reconstructed ESI+ and ESI− mass spectra of the assigned *m/z* for (a) QOMS and (b) WLG. The Venn diagram in each figure show the comparison of identified formula between ESI+ and ESI− modes; the pie charts in each figure show the ratio of assigned formula to total MS peaks detected in each mode. The abundance weighted (w) elemental ratios are shown.

Table 1
The Most Abundant Five Peaks in Each Mode at the Two Sites

Site	Experimental m/z	Elemental formula of neutral species	Relative abundance	DBE	Detection mode
QOMS	118.07380	$C_4H_{10}N_2O_2$	31.9	1	(+)ESI
	119.09402	$C_5H_{13}NO_2$	4.0	0	(+)ESI
	89.04764	$C_3H_7NO_2$	3.7	1	(+)ESI
	117.07860	$C_5H_{11}NO_2$	3.3	1	(+)ESI
	134.06852	$C_4H_{10}N_2O_3$	2.6	1	(+)ESI
	168.02682	$C_4H_8O_7$	17.4	1	(−)ESI
	164.04687	$C_9H_8O_3$	2.5	6	(−)ESI
	153.04216	$C_7H_7NO_3$	2.0	5	(−)ESI
	200.10468	$C_{10}H_{16}O_4$	1.4	3	(−)ESI
	180.04196	$C_9H_8O_4$	1.3	6	(−)ESI
WLG	302.11414	$C_{17}H_{18}O_5S$	11.5	9	(+)ESI
	370.21817	$C_{16}H_{34}O_9S$	2.8	0	(+)ESI
	414.24426	$C_{18}H_{38}O_{10}S$	2.3	0	(+)ESI
	326.19251	$C_{14}H_{30}O_8S$	2.3	0	(+)ESI
	428.25959	$C_{19}H_{40}O_{10}S$	1.9	0	(+)ESI
	188.06812	$C_8H_{12}O_5$	13.9	3	(−)ESI
	202.08389	$C_9H_{14}O_5$	3.9	3	(−)ESI
	174.05240	$C_7H_{10}O_5$	3.2	3	(−)ESI
	139.02635	$C_6H_5NO_3$	2.8	5	(−)ESI
	200.10461	$C_{10}H_{16}O_4$	2.2	3	(−)ESI

(5369 for QOMS and 3600 for WLG). Out of them, ~18% species were observed in both (+)ESI and (−)ESI modes, for each site (Figures 8a and 8b). Larger fractions of species with higher m/z values were detected in the WLG samples, compared to the QOMS. The m/z in the QOMS samples were mainly in the range of 100–200, while in the WLG sample they were in the range of 200–400. The identified molecular formulas were further categorized into CHO, CHON, CHONS, and CHOS subclasses based on their elemental composition (Figure S4). Table 1 summarizes the chemical composition of five most abundant peaks detected in each mode for these two sites. In the (+)ESI mode, CHOS compounds dominate the most abundant peaks in the WLG samples, while CHON compounds dominate the most abundant peaks in the QOMS samples. In (−)ESI mode, CHO compounds are the major species detected at both sites.

The differences in chemical characteristics between the QOMS and WLG samples can be additionally illustrated through elemental ratios. The abundance weighted O/C in (+)ESI and (−)ESI modes of the QOMS samples were 0.42 and 0.65, which were higher than those of the WLG samples (0.39 and 0.49), respectively, suggesting its higher oxidation degree. Oxidation state of carbon (OSC), a more specific metric for oxidation of OA, shows −0.70 and −0.79 for the QOMS and the WLG samples, indicating higher oxidation state of OA at QOMS. The plot of OSC vs. number of carbon atoms (n_C) show high clustering of points at oxygenated OA (OOA) for QOMS than WLG (Figure 9). This higher oxidation degree of OA at QOMS was also observed in previous AMS measurements (Zhang et al., 2018; Zhang et al., 2019). The Van Krevelen (VK) diagram plots

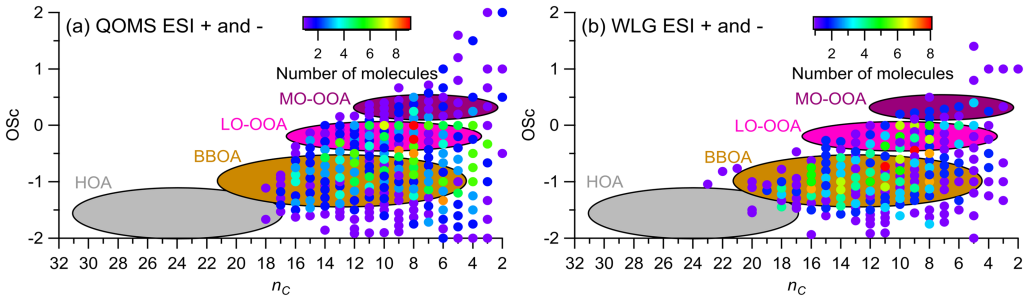

Figure 9. The plot of carbon-based oxidation state (OSC) vs. number of carbon atom (n_C) for (a) QOMS and (b) WLG colored by the distribution of number of molecules. The circles in each plot indicate the potential organic aerosol sources. Hydrocarbon-like organic aerosol (HOA) and biomass burning organic aerosol (BBOA) correspond to primary particulate matter directly emitted into the atmosphere. Less and more oxidized organic aerosol (LO-OOA and MO-OOA) correspond to fresh and aged secondary aerosol produced by multistep oxidation reactions.

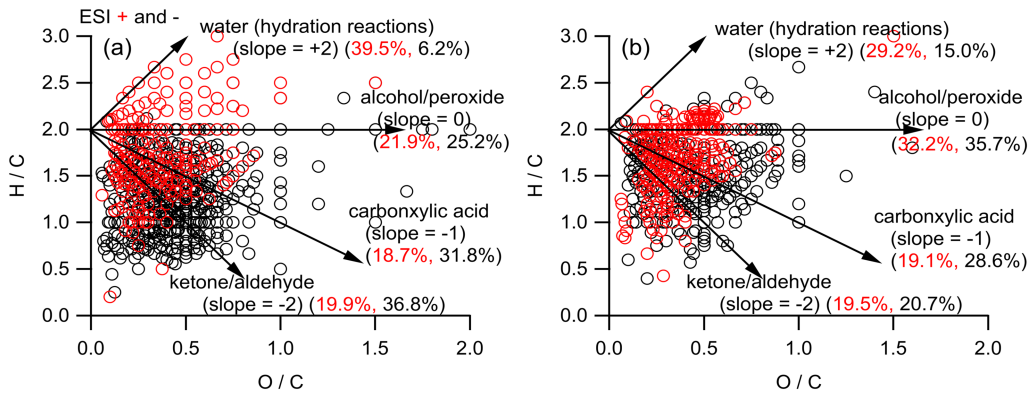

Figure 10. Van Krevelen diagram of H/C vs. O/C for (a) QOMS and (b) WLG. Data points from ESI+ are marked in red and ESI- are marked in black. Each arrow corresponds to the addition of a particular functional group to an aliphatic carbon and the percentage number indicate the data points in each region to the total data points.

the hydrogen to carbon atomic ratio (H/C) and the oxygen to carbon atomic ratio (O/C). It can be used to infer plausible functional groups contained in the species and further deduce the reaction pathways of which they form (Heald et al., 2010). The VK diagrams for the aerosol samples from the QOMS and WLG sites are shown in Figure 10. Molecules in the QOMS samples may have higher extent of carbonyl functional groups (slope < -1) than those of the WLG sample. This suggests that the species in the QOMS sample contain more unsaturated compounds than those from the WLG sample. Indeed, the abundance weighted DBE in (−)ESI was 5.62 for the QOMS and 4.36 for the WLG samples.

The plot of DBE vs. n_C can be used to infer the distribution of potential BrC active components (Lin et al., 2018). Since light absorption of BrC requires conjugated double bonds, the potential chromophores are suggested to have DBE/C ratio greater than that of linear polyenes (Lin et al., 2018), which is highlighted in brown in Figure 11. It is distinct that OA species from the QOMS sample have higher DBE values, and corresponding species were detected in both (+)ESI and (−)ESI modes (66 + 339 for the QOMS vs. 29 + 132 for the WLG samples, respectively), with more species detected in (−)ESI mode. These species with high DBE values are mainly CHO and CHON compounds (190 vs. 149 for QOMS (−)ESI; 22 vs. 44 for QOMS (+)ESI; 102 vs. 30 for WLG (−)ESI; 24 vs. 5 for WLG (+)ESI). The tentative structures of these CHO compounds are suggested to be lignin fragments and molecular markers of biomass burning, which is a significant source of OA in this region (Zhang et al., 2018). These CHO compounds are relatively small aromatic compounds with 8–11 C atoms and multiple acidic polar functional groups, which are readily ionized in the (−)ESI mode. In contrast, biomass burning is not a major contributor to OA in the WLG samples, which is likely the major reason for less distinct BrC chromophores observed in the WLG samples compared to the QOMS (Zhang et al., 2019). In addition, 149 and 30 nitrogen-containing potential BrC chromophores were detected in the QOMS and the WLG samples, respectively, in the (−)ESI mode. These nitrogen-containing compounds contained 1 or 2 N atoms and 2–4 O atoms, and likely are nitrophenols originated from biomass burning emissions. Reactions of nitrogen dioxide (NO_2) and nitrate radicals (NO_3) with phenolic compounds in biomass burning plume could be the potential formation pathways of these compounds.

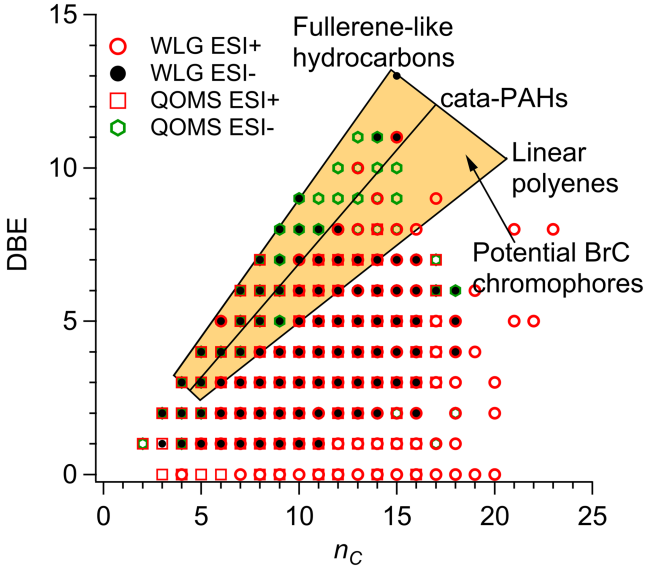

Figure 11. The plot of DBE vs. n_C. The reference lines indicate linear polyene (DBE = 0.5 * n_C), cata-PAHs (DBE = 0.75 * n_C − 0.5), and fullerene-like hydrocarbons (DBE = 0.9 * n_C). The brown highlighted region represents potential brown carbon chromophores. Note that many points are overlapped together.

3.3. Potential Aerosol Sources and Chemical Processes in These Two Sites

Different chemical and physical properties of OA sampled at the QOMS and WLG sites suggest that the aerosol sources and chemical processes in these two regions are different. Aerosol sources for these two sites

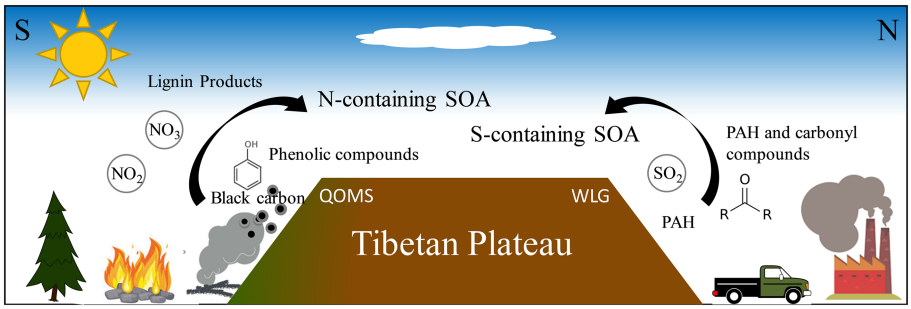

Figure 12. Concept mode of atmospheric chemical processes in the southern and northern Tibetan Plateau.

could be generally determined by air mass trajectory analysis which show that the air mass to WLG were all from the inland of northwest of China with about 50% from the source at short distance (100–200 km), while they were dominantly from northwest of India with long distance (up to 1,000 km) (Figure S5). Based on satellite monitoring and in situ observations (Kumar et al., 2011; Zhang et al., 2018), biomass burning has been identified as the major source of OA in the southern TP, while anthropogenic emissions (coal combustion and fossil fuel usage) are the major source of OA in the northern TP (Li et al., 2016) (Figure 12). This is determined by the energy structure and distribution of natural resources in the countries adjacent to the northern and southern part of the TP region. For example, use of wood for residential cooking and heating is very common in India, while coal is more widely used in China. Combustion of coal emits large amounts of sulfur dioxide (SO_2), carbonyl compounds, and PAH (Chen et al., 2005; Jakober et al., 2006). Under the urbanization and economic development in Western China, SO_2 emissions show an increasing trend in contrast to the decreasing trend in East China (Ling et al., 2017). High concentration of SO_2 with carbonyl compounds and PAH is susceptible to form sulfur-containing SOA (Hettiyadura et al., 2017; Staudt et al., 2014). Biomass burning emits large amount of nitrogen oxides (NO and NO_2; NO_x), and reactive volatile organic compounds such as phenolic compounds (Andreae & Merlet, 2001; Simoneit et al., 1993). In addition, high contribution of nitrate is generally observed in biomass burning emission plume, as reported by the AMS measurement at the QOMS site (Zhang et al., 2018). Reactions of NO_x and NO_3 with phenolic compounds can generate light absorbing BrC compounds, such as nitro-phenols (Lin et al., 2016).

4. Conclusions

The chemical composition and mass loading of $PM_{2.5}$ samples collected at the QOMS and the WLG sites are substantially different. Specifically, sulfate is the major constituent of $PM_{2.5}$ at the WLG, while OA is the major constituent of $PM_{2.5}$ at the QOMS. The light absorption by OA at the QOMS site is stronger than that at the WLG site, suggesting higher content of atmospheric BrC at the QOMS site, compared to the WLG. The light absorption of OA at the QOMS site is pH dependent. The weak susceptibility of the OA to photolysis at both sites suggests presence of aged OA at both sites. The elemental composition analysis indicates high contribution of CHON compounds in the QOMS samples and CHOS compounds in the WLG samples. Likely, the CHON compounds originated from biomass burning emissions, while CHOS compounds originated from anthropogenic emissions. The underlined differences in the chemical composition and light absorption properties of aerosols in the southern and northern TP in this study should be taken into account to accurately predict the radiative forcing in different regions in climate models.

Acknowledgments
This research was supported by grants from the National Natural Science Foundation of China (41771079; 41977189), the Strategic Priority Research Program of Chinese Academy of Sciences, Pan-Third Pole Environment Study for a Green Silk Road (Pan-TPE) (XDA20040501), and the Chinese Academy of Sciences Hundred Talents Program. APSH and AL acknowledge support by the U.S. Department of Commerce, National Oceanic and Atmospheric Administration through Climate Program Office's AC4 program, award NA16OAR4310101. The data in this manuscript are available at https://zenodo.org/record/3517312#.XeexmdVOkuU (DOI: 10.5281/zenodo.3517312). We would like to thank the NASA team for providing MODIS (https://worldview.earthdata.nasa.gov) and the NOAA Air Resources Laboratory team for the open access on HYSPLIT trajectory model (https://ready.arl.noaa.gov/HYSPLIT-traj.php). We also would like to thank Dr. Yange Zhang for IC and OC/EC analysis.

References

Andreae, M. O., & Merlet, P. (2001). Emission of trace gases and aerosols from biomass burning. *Global Biogeochemical Cycles*, *15*(4), 955–966. https://doi.org/10.1029/2000gb001382

Bein, K. J., & Wexler, A. S. (2014). A high-efficiency, low-bias method for extracting particulate matter from filter and impactor substrates. *Atmospheric Environment*, *90*, 87–95. https://doi.org/10.1016/j.atmosenv.2014.03.042

Bonasoni, P., Laj, P., Marinoni, A., Sprenger, M., Angelini, F., Arduini, J., et al. (2010). Atmospheric Brown Clouds in the Himalayas: First two years of continuous observations at the Nepal Climate Observatory-Pyramid (5079 m). *Atmospheric Chemistry and Physics*, *10*(15), 7515–7531. https://doi.org/10.5194/acp-10-7515-2010

Cai, J., Zhi, G., Yu, Z., Nie, P., Gligorovski, S., Zhang, Y., et al. (2018). Spectral changes induced by pH variation of aqueous extracts derived from biomass burning aerosols: Under dark and in presence of simulated sunlight irradiation. *Atmospheric Environment*, *185*, 1–6. https://doi.org/10.1016/j.atmosenv.2018.04.037

Cao, J.-J., Xu, B.-Q., He, J.-Q., Liu, X.-Q., Han, Y.-M., Wang, G.-H., & Zhu, C.-S. (2009). Concentrations, seasonal variations, and transport of carbonaceous aerosols at a remote Mountainous region in western China. *Atmospheric Environment*, *43*(29), 4444–4452. https://doi.org/10.1016/j.atmosenv.2009.06.023

Chen, Y. J., Sheng, G. Y., Bi, X. H., Feng, Y. L., Mai, B. X., & Fu, J. M. (2005). Emission factors for carbonaceous particles and polycyclic aromatic hydrocarbons from residential coal combustion in China. *Environmental Science & Technology*, *39*(6), 1861–1867. https://doi.org/10.1021/es0493650

Desyaterik, Y., Sun, Y., Shen, X., Lee, T., Wang, X., Wang, T., & Collett, J. L. Jr. (2013). Speciation of "brown" carbon in cloud water impacted by agricultural biomass burning in eastern China. *Journal of Geophysical Research: Atmospheres*, *118*, 7389–7399. https://doi.org/10.1002/jgrd.50561

Du, Z. Y., He, K. B., Cheng, Y., Duan, F. K., Ma, Y. L., Liu, J. M., et al. (2014). A yearlong study of water-soluble organic carbon in Beijing II: Light absorption properties. *Atmospheric Environment*, *89*, 235–241. https://doi.org/10.1016/j.atmosenv.2014.02.022

Feng, L., Xu, J., Kang, S., Li, X., Li, Y., Jiang, B., & Shi, Q. (2016). Chemical composition of microbe-derived dissolved organic matter in cryoconite in Tibetan Plateau glaciers: Insights from Fourier transform ion cyclotron resonance mass spectrometry analysis. *Environmental Science & Technology*, *50*(24), 13215–13223. https://doi.org/10.1021/acs.est.6b03971

Fleming, L. T., Lin, P., Roberts, J. M., Selimovic, V., Yokelson, R., Laskin, J., et al. (2019). Molecular composition and photochemical lifetimes of brown carbon chromophores in biomass burning organic aerosol. *Atmospheric Chemistry and Physics Discussions*, *2019*, 1–38. https://doi.org/10.5194/acp-2019-523

Heald, C. L., Kroll, J. H., Jimenez, J. L., Docherty, K. S., DeCarlo, P. F., Aiken, A. C., et al. (2010). A simplified description of the evolution of organic aerosol composition in the atmosphere. *Geophysical Research Letters*, *37*, L08803. https://doi.org/10.1029/2010gl042737

Hegde, P., & Kawamura, K. (2012). Seasonal variations of water-soluble organic carbon, dicarboxylic acids, ketocarboxylic acids, and α-dicarbonyls in Central Himalayan aerosols. *Atmospheric Chemistry and Physics*, *12*(14), 6645–6665. https://doi.org/10.5194/acp-12-6645-2012

Hettiyadura, A. P. S., Jayarathne, T., Baumann, K., Goldstein, A. H., de Gouw, J. A., Koss, A., et al. (2017). Qualitative and quantitative analysis of atmospheric organosulfates in Centreville, Alabama. *Atmospheric Chemistry and Physics*, *17*(2), 1343–1359. https://doi.org/10.5194/acp-17-1343-2017

Huang, J., Minnis, P., Yi, Y., Tang, Q., Wang, X., Hu, Y., et al. (2007). Summer dust aerosols detected from CALIPSO over the Tibetan Plateau. *Geophysical Research Letters*, *34*, L18805. https://doi.org/10.1029/2007GL029938

Jakober, C. A., Charles, M. J., Kleeman, M. J., & Green, P. G. (2006). LC—MS analysis of carbonyl compounds and their occurrence in diesel emissions. *Analytical Chemistry*, *78*(14), 5086–5093. https://doi.org/10.1021/ac060301c

Jo, D. S., Park, R. J., Lee, S., Kim, S. W., & Zhang, X. (2016). A global simulation of brown carbon: implications for photochemistry and direct radiative effect. *Atmospheric Chemistry and Physics*, *16*(5), 3413–3432. https://doi.org/10.5194/acp-16-3413-2016

Kirillova, E. N., Marinoni, A., Bonasoni, P., Vuillermoz, E., Facchini, M. C., Fuzzi, S., & Decesari, S. (2016). Light absorption properties of brown carbon in the high Himalayas. *Journal of Geophysical Research: Atmospheres*, *121*, 9621–9639. https://doi.org/10.1002/2016JD025030

Kumar, R., Naja, M., Satheesh, S. K., Ojha, N., Joshi, H., Sarangi, T., et al. (2011). Influences of the springtime northern Indian biomass burning over the central Himalayas. *Journal of Geophysical Research*, *116*(D19), D19302. https://doi.org/10.1029/2010JD015509

Kuwata, M., Zorn, S. R., & Martin, S. T. (2011). Using elemental ratios to predict the density of organic material composed of carbon, hydrogen, and oxygen. *Environmental Science & Technology*, *46*(2), 787–794. https://doi.org/10.1021/es202525q

Laskin, A., Laskin, J., & Nizkorodov, S. A. (2015). Chemistry of atmospheric brown carbon. *Chemical Reviews*, *115*(10), 4335–4382. https://doi.org/10.1021/cr5006167

Laskin, J., Laskin, A., & Nizkorodov, S. A. (2018). Mass Spectrometry Analysis in Atmospheric Chemistry. *Analytical Chemistry*, *90*, 166–189. https://doi.org/10.1021/acs.analchem.7b04249

Lau, K. M., Kim, M. K., & Kim, K. M. (2006). Asian summer monsoon anomalies induced by aerosol direct forcing: The role of the Tibetan Plateau. *Climate Dynamics*, *26*(7-8), 855–864. https://doi.org/10.1007/s00382-006-0114-z

Li, C., Bosch, C., Kang, S., Andersson, A., Chen, P., Zhang, Q., et al. (2016). Sources of black carbon to the Himalayan–Tibetan Plateau glaciers. *Nature Communications*, *7*, 12574. https://doi.org/10.1038/ncomms12574

Lin, P., Aiona, P. K., Li, Y., Shiraiwa, M., Laskin, J., Nizkorodov, S. A., & Laskin, A. (2016). Molecular characterization of brown carbon in biomass burning aerosol particles. *Environmental Science & Technology*, *50*(21), 11,815–11,824. https://doi.org/10.1021/acs.est.6b03024

Lin, P., Bluvshtein, N., Rudich, Y., Nizkorodov, S. A., Laskin, J., & Laskin, A. (2017). Molecular chemistry of atmospheric brown carbon inferred from a nationwide biomass burning event. *Environmental Science & Technology*, *51*(20), 11,561–11,570. https://doi.org/10.1021/acs.est.7b02276

Lin, P., Fleming, L. T., Nizkorodov, S. A., Laskin, J., & Laskin, A. (2018). Comprehensive molecular characterization of atmospheric brown carbon by high resolution mass spectrometry with electrospray and atmospheric pressure photoionization. *Analytical Chemistry*, *90*(21), 12,493–12,502. https://doi.org/10.1021/acs.analchem.8b02177

Ling, Z., Huang, T., Zhao, Y., Li, J., Zhang, X., Wang, J., et al. (2017). OMI-measured increasing SO_2 emissions due to energy industry expansion and relocation in northwestern China. *Atmospheric Chemistry and Physics*, *17*(14), 9115–9131. https://doi.org/10.5194/acp-17-9115-2017

Liu, J., Bergin, M., Guo, H., King, L., Kotra, N., Edgerton, E., & Weber, R. J. (2013). Size-resolved measurements of brown carbon in water and methanol extracts and estimates of their contribution to ambient fine-particle light absorption. *Atmospheric Chemistry and Physics*, *13*(24), 12,389–12,404. https://doi.org/10.5194/acp-13-12389-2013

Liu, Z., Liu, D., Huang, J., Vaughan, M., Uno, I., Sugimoto, N., et al. (2008). Airborne dust distributions over the Tibetan Plateau and surrounding areas derived from the first year of CALIPSO Lidar observations. *Atmospheric Chemistry and Physics*, *8*(16), 5045–5060. https://doi.org/10.5194/acp-8-5045-2008

Lüthi, Z. L., Škerlak, B., Kim, S. W., Lauer, A., Mues, A., Rupakheti, M., & Kang, S. (2015). Atmospheric brown clouds reach the Tibetan Plateau by crossing the Himalayas. *Atmospheric Chemistry and Physics*, *15*(11), 6007–6021. https://doi.org/10.5194/acp-15-6007-2015

Marcq, S., Laj, P., Roger, J. C., Villani, P., Sellegri, K., Bonasoni, P., et al. (2010). Aerosol optical properties and radiative forcing in the high Himalaya based on measurements at the Nepal Climate Observatory-Pyramid site (5079 m a.s.l.). *Atmospheric Chemistry and Physics*, *10*(13), 5859–5872. https://doi.org/10.5194/acp-10-5859-2010

Ming, J., Xiao, C., Sun, J., Kang, S., & Bonasoni, P. (2010). Carbonaceous particles in the atmosphere and precipitation of the Nam Co region, central Tibet. *Journal of Environmental Sciences*, *22*(11), 1748–1756. https://doi.org/10.1016/S1001-0742(09)60315-6

Olson, M. R., Victoria Garcia, M., Robinson, M. A., Van Rooy, P., Dietenberger, M. A., Bergin, M., & Schauer, J. J. (2015). Investigation of black and brown carbon multiple-wavelength-dependent light absorption from biomass and fossil fuel combustion source emissions. *Journal of Geophysical Research: Atmospheres*, *120*, 6682–6697. https://doi.org/10.1002/2014JD022970

Phillips, S. M., Bellcross, A. D., & Smith, G. D. (2017). Light Absorption by brown carbon in the southeastern United States is pH-dependent. *Environmental Science & Technology*, *51*(12), 6782–6790. https://doi.org/10.1021/acs.est.7b01116

Ramanathan, V., Ramana, M. V., Roberts, G., Kim, D., Corrigan, C., Chung, C., & Winker, D. (2007). Warming trends in Asia amplified by brown cloud solar absorption. *Nature*, *448*(7153), 575–578. https://doi.org/10.1038/nature06019

Roach, P. J., Laskin, J., & Laskin, A. (2011). Higher-order mass defect analysis for mass Spectra of complex organic mixtures. *Analytical Chemistry*, *83*(12), 4924–4929. https://doi.org/10.1021/ac200654j

Simoneit, B. R. T., Rogge, W. F., Mazurek, M. A., Standley, L. J., Hildemann, L. M., & Cass, G. R. (1993). Lignin pyrolysis products, lignans, and resin acids as specific tracers of plant classes in emissions from biomass combustion. *Environmental Science & Technology*, *27*(12), 2533–2541. https://doi.org/10.1021/es00048a034

Staudt, S., Kundu, S., Lehmler, H.-J., He, X., Cui, T., Lin, Y.-H., et al. (2014). Aromatic organosulfates in atmospheric aerosols: Synthesis, characterization, and abundance. *Atmospheric Environment*, *94*, 366–373. https://doi.org/10.1016/j.atmosenv.2014.05.049

Washenfelder, R. A., Attwood, A. R., Brock, C. A., Guo, H., Xu, L., Weber, R. J., et al. (2015). Biomass burning dominates brown carbon absorption in the rural southeastern United States. *Geophysical Research Letters*, *42*, 653–664. https://doi.org/10.1002/2014GL062444

Xie, M., Chen, X., Hays, M. D., Lewandowski, M., Offenberg, J., Kleindienst, T. E., & Holder, A. L. (2017). Light absorption of secondary organic aerosol: composition and contribution of nitroaromatic compounds. *Environmental Science & Technology*, *51*(20), 11,607–11,616. https://doi.org/10.1021/acs.est.7b03263

Xu, J., Wang, Z., Yu, G., Qin, X., Ren, J., & Qin, D. (2014). Characteristics of water soluble ionic species in fine particles from a high altitude site on the northern boundary of Tibetan Plateau: Mixture of mineral dust and anthropogenic aerosol. *Atmospheric Research*, *143*, 43–56. https://doi.org/10.1016/j.atmosres.2014.01.018

Xu, J., Wang, Z., Yu, G., Sun, W., Qin, X., Ren, J., & Qin, D. (2013). Seasonal and diurnal variations in aerosol concentrations at a high-altitude site on the northern boundary of Qinghai-Xizang Plateau. *Atmospheric Research*, *120–121*, 240–248. https://doi.org/10.1016/j.atmosres.2012.08.022

Xu, J., Zhang, Q., Shi, J., Ge, X., Xie, C., Wang, J., et al. (2018). Chemical characteristics of submicron particles at the central Tibetan Plateau: Insights from aerosol mass spectrometry. *Atmospheric Chemistry and Physics*, *18*(1), 427–443. https://doi.org/10.5194/acp-18-427-2018

Xu, J., Zhang, Q., Wang, Z. B., Yu, G. M., Ge, X. L., & Qin, X. (2015). Chemical composition and size distribution of summertime $PM_{2.5}$ at a high altitude remote location in the northeast of the Qinghai–Xizang (Tibet) Plateau: Insights into aerosol sources and processing in free troposphere. *Atmospheric Chemistry and Physics*, *15*(9), 5069–5081. https://doi.org/10.5194/acp-15-5069-2015

Yanai, M., & Wu, G.-X. (2006). Effects of the Tibetan Plateau. In *The Asian Monsoon, edited* (pp. 513–549). Berlin Heidelberg, Berlin, Heidelberg: Springer. https://doi.org/10.1007/3-540-37722-0_13

Zhang, N., Cao, J., Liu, S., Zhao, Z., Xu, H., & Xiao, S. (2014). Chemical composition and sources of $PM_{2.5}$ and TSP collected at Qinghai Lake during summertime. *Atmospheric Research*, *138*, 213–222. https://doi.org/10.1016/j.atmosres.2013.11.016

Zhang, X., Lin, Y.-H., Surratt, J. D., Zotter, P., Prévôt, A. S. H., & Weber, R. J. (2011). Light-absorbing soluble organic aerosol in Los Angeles and Atlanta: A contrast in secondary organic aerosol. *Geophysical Research Letters*, *38*(21), L21810. https://doi.org/10.1029/2011gl049385

Zhang, X., Xu, J., Kang, S., Liu, Y., & Zhang, Q. (2018). Chemical characterization of long-range transport biomass burning emissions to the Himalayas: Insights from high-resolution aerosol mass spectrometry. *Atmospheric Chemistry and Physics*, *18*(7), 4617–4638. https://doi.org/10.5194/acp-18-4617-2018

Zhang, X., Xu, J., Kang, S., Zhang, Q., & Sun, J. (2019). Chemical characterization and sources of submicron aerosols in the northeastern Qinghai–Tibet Plateau: Insights from high-resolution mass spectrometry. *Atmospheric Chemistry and Physics*, *19*(11), 7897–7911. https://doi.org/10.5194/acp-19-7897-2019

Zhang, Y., Forrister, H., Liu, J., Dibb, J., Anderson, B., Schwarz, J. P., et al. (2017). Top-of-atmosphere radiative forcing affected by brown carbon in the upper troposphere. *Nature Geoscience*, *10*(7), 486–489. https://doi.org/10.1038/ngeo2960

Zhu, C.-S., Cao, J.-J., Huang, R.-J., Shen, Z.-X., Wang, Q.-Y., & Zhang, N.-N. (2018). Light absorption properties of brown carbon over the southeastern Tibetan Plateau. *Science of the Total Environment*, *625*, 246–251. https://doi.org/10.1016/j.scitotenv.2017.12.183